ACS APPLIED NANO MATERIALS

www.acsanm.org Article

Nanoscale Studies at the Early Stage of Water-Induced Degradation of $CH_3NH_3PbI_3$ Perovskite Films Used for Photovoltaic Applications

Jaume Llacer, David Moerman, Olivier Douhéret, Xavier Noirfalise, Claudio Quarti, Roberto Lazzaroni, Didier Théron, and Philippe Leclère*

Cite This: *ACS Appl. Nano Mater.* 2020, 3, 8268–8277 Read Online

ACCESS | Metrics & More | Article Recommendations | Supporting Information

ABSTRACT: Understanding the surface properties of hybrid perovskite materials is a key aspect to improve not only the interface properties in photovoltaic cells but also the stability against moisture degradation. In this work, we study the local electronic properties of two series of $CH_3NH_3PbI_3$ perovskite films by atomic force microscopy-based methods. We correlate nanoscale features such as the local surface potential (as measured by Kelvin probe force microscopy) to the current response (as measured by conductive atomic force microscopy). $CH_3NH_3PbI_3$ perovskites made using lead acetate as a precursor result in films with high purity and crystallinity and also result in heterogeneous local electrical properties, attributed to variations in the density of surface states. In contrast, when using lead iodide as a precursor, the perovskite surface exhibits a uniform distribution of surface states. This work also aims to understand the early stages of water-induced degradation at the surface of those films. Through high-precision exposure to small amounts of water vapor, we observe a higher stability for surfaces prepared with lead iodide precursors. More importantly, each precursor-based fabrication route is associated with either n- or p-type behavior of the films. These characteristics are determined by the type of surface states, which also and eventually preside over stability. This work should help discriminate between perovskite synthesis routes and improve their stability in photovoltaic cell applications.

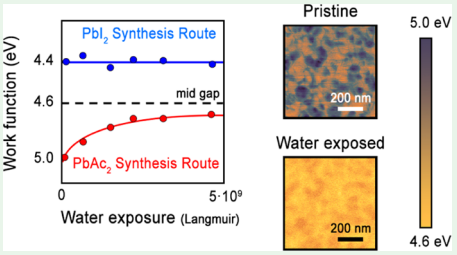

KEYWORDS: *hybrid perovskite, defects, stability, kelvin probe force microscopy, surface properties*

1. INTRODUCTION

Organic–inorganic hybrid perovskites have been capturing much interest in the field of photovoltaics (PV) as the power conversion efficiencies (PCEs) of corresponding devices have been strongly improved, from 3.8% in 2009 to more than 23% recently.[1,2] This prodigious increase in just a decade is the result of intense research and fundamental understanding of crucial intrinsic properties of the perovskites; in particular, their electronic and charge transport properties feature remarkably long diffusion lengths and carrier lifetimes (refs 3–8).[3−8] However, the device stability and the mechanisms responsible for this low stability are still under debate.[9,10] In addition to the bulk properties, the surface properties at the nanoscale, which depend on the crystallographic facets and the possible presence of defects, are also of prime importance as their impact on electronic and transport properties at grain boundaries or other interfaces is significant, hence affecting the performances of the devices.[11−18]

Several methods are proposed for reducing these detrimental effects for photovoltaic performances, involving, among others, tuning of the perovskite composition and interfacial engineering.[19−21] For instance, reducing the recombination at the interface can be achieved by introducing a chemical linker between the perovskite and the electron transport layer.[22] Recombination sites were also reduced after passivation of grain boundaries using either an excess of methylammonium iodide (MAI) during the synthesis or a postfabrication surface treatment.[23,24]

Yet, to address such a major issue, the electronic properties on the surface of perovskite thin films ought to be further investigated where variations can be observed, *i.e.*, at the nanoscale. In this regard, scanning probe microscopy (SPM) provides several characterization methods to locally map the electronic properties of materials with nanometer resolution.[25−31] Kim et al. recently used Kelvin probe force microscopy (KPFM) and bias-dependent atomic force microscopy (AFM) to show that the properties on the (112) surface of a perovskite crystal can be affected upon external bias while the (100) surface remains unchanged.[32] KPFM has also been used by many other groups to study the surface potential of perovskite thin films: Bergmann et al. used cross-section KPFM on an $MAPbI_3$-based solar cell to show the unbalanced charge-carrier extraction between electrons and

Received: June 19, 2020
Accepted: August 7, 2020
Published: August 7, 2020

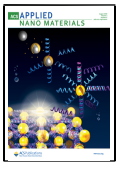

https://dx.doi.org/10.1021/acsanm.0c01687
ACS Appl. Nano Mater. 2020, 3, 8268–8277

holes.[27] Harwell et al. exposed the $MAPbI_3$ perovskite repeatedly to light and found that the Fermi level eventually returns with time to its initial value with slow decay, this effect being attributed to trapped or slow charges within the device.[33] Stecker et al. used SPM to identify vacancy-assisted transport and, combined with density functional theory (DFT) calculations, they predicted an increase in the work function when increasing the number of vacancies in $MAPbBr_3$.[34] Gallet et al. found electronic heterogeneities at the $MAPbI_3$ perovskite surface and attributed them to differences in surface terminations.[35]

From these works, it has been mostly agreed that among the surface features ruling the electronic properties of the perovskite, defects or traps are those responsible for the electronic heterogeneities observed at the local scale. Traps can be classified as shallow or deep, depending on the energy position in the gap. Calculations on the activation energies of all possible point defects as determined from those studies revealed that usually shallow trap states are more likely to form than deep traps, and they can be an explanation for the long electron−hole diffusion lengths observed in these materials.[36] Yet, Du et al. identified iodine interstitials, with specifically low activation energies that could generate significant deep trap states.[37] In addition, all of these studies also point out how the type and density of traps at the surface of the perovskite depend on the growth conditions of the materials along with the anisotropy of the surface properties.

In spite of different types of defects evidenced at the surface, their corresponding impact on film stability is still under debate. To enhance perovskite stability, it is therefore crucial to understand how these defects specifically affect the surface properties and how they interact with water molecules, especially at the early stage of degradation.

In this work, frequency-modulated KPFM (FM-KPFM) and conductive atomic force microscopy (C-AFM) are first used to evidence the presence and the electronic contribution of trap states at the surface of methylammonium lead iodide ($CH_3NH_3PbI_3$ or $MAPbI_3$) perovskite thin films. FM-KPFM is an appropriate method to simultaneously probe topographic and surface potential variations without cross-talking.[25,29] It measures the contact potential difference (CPD, *i.e.*, the work function difference) between the metallic probe and the sample under test, hence providing meaningful insights toward device performances and stability.[38] C-AFM was also shown to be pertinent for high-resolution electrical characterization of perovskites.[39] As a current measurement method, C-AFM can be sensitive to contributions from surface properties, such as defects, as they are expected to impact the charge transport mechanism *via* carrier injection.[23,39,40] Combining FM-KPFM and C-AFM allows us to locally correlate carrier injection to work function (WF) in view of understanding the electronic properties of the sample surface.

Further on, the early stages of perovskite degradation upon water vapor exposure are studied at the nanoscale. Typically, the stability of perovskite films and devices as reported in the literature has been studied after exposing the samples to ambient conditions at different humidity levels. Here, we introduce a more precise method allowing for controlled exposure to low-level water exposure. For this study, $MAPbI_3$ was prepared by two different synthesis routes, either lead acetate-based ($PbAc_2$) or lead iodide-based (PbI_2); see Scheme 1a. The SPM measurements, carried out for both sets of samples, exhibit different surface electronic properties

Scheme 1. (a) $MAPbI_3$ Perovskite Deposition Processes: MAPI-$PbAc_2$ and MAPI-PbI_2, (b) Schematic of the KPFM Measurement System for Each $MAPbI_3$ Film, and (c) Schematic of the $MAPbI_3$ Structure

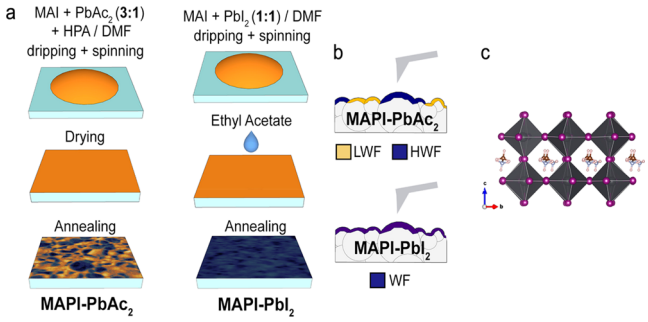

and stabilities upon exposure to water; see Scheme 1b. Complementary X-ray photoelectron spectroscopy (XPS) and X-ray diffraction (XRD) analyses correlate the observations with the variations in the chemical composition and the crystalline orientation planes, respectively, for the two types of $MAPbI_3$ perovskites; see the chemical structure of $MAPbI_3$ in Scheme 1c. Consistent pictures can be drawn between chemical structure and composition, surface states and electronic properties and water stability for each of the two differently synthesized perovskites, which can ultimately help improve the device performance.

2. RESULTS AND DISCUSSION

2.1. Local Heterogeneity at the Surface of $MAPbI_3$ Perovskites. The first set of perovskites studied consisted of $MAPbI_3$ films deposited on top of a glass/ITO/PEDOT:PSS substrate, using $PbAc_2$ as a precursor and following the fabrication procedure described in Section 4. This material will be referred to as MAPI-$PbAc_2$.[41,42] Freshly prepared MAPI-$PbAc_2$ thin films were analyzed by XRD and XPS to determine their chemical composition and crystallinity, respectively, to establish reference profiles prior to any degradation process, and to confirm standards reported in the literature for pristine $MAPbI_3$. As shown by the XPS spectrum of Figure 1a, the major atomic species present at the surface of MAPI-$PbAc_2$ are, as expected, iodine, nitrogen, carbon, and lead. The additional presence of indium atoms could be attributed to the presence of pinholes in the PEDOT:PSS + $MAPbI_3$ stack.[43] The corresponding XRD profile, displayed in Figure 1b, indicates a dominating presence of (110) and equivalent (220) crystalline planes corroborating the high crystal orientation expected from this fabrication route.[44] Moreover, the characteristic peak of PbI_2 expected at ∼12.6° (see the asterisk symbol in Figure 1b), and usually related to perovskite phase segregation, is absent, allowing these XRD and XPS data to serve as reference profiles for pristine MAPI-$PbAc_2$.[45] The corresponding morphology of the films is composed of grains of varying sizes (170 ± 130 nm in diameter), as determined by noncontact AFM (Figure 1c) operated in an inert environment. The topography of the films reports a typical root-mean-square (RMS) roughness of around 34 nm for 4 × 4 μm^2 images.

Figure 2a,c shows the topography and WF, respectively, as measured by FM-KPFM for an MAPI-$PbAc_2$ film deposited on a glass/ITO/PEDOT:PSS substrate (the WF image was obtained from the surface potential data after tip calibration;

https://dx.doi.org/10.1021/acsanm.0c01687
ACS Appl. Nano Mater. 2020, 3, 8268−8277

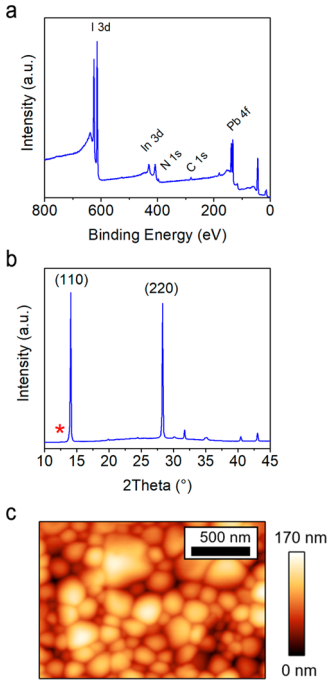

Figure 1. Characterization of freshly prepared MAPI-$PbAc_2$ deposits: (a) XPS survey spectrum, (b) X-ray diffractogram (the asterisk symbol indicates the angle corresponding to the reflection expected for PbI_2), and (c) typical noncontact AFM height image.

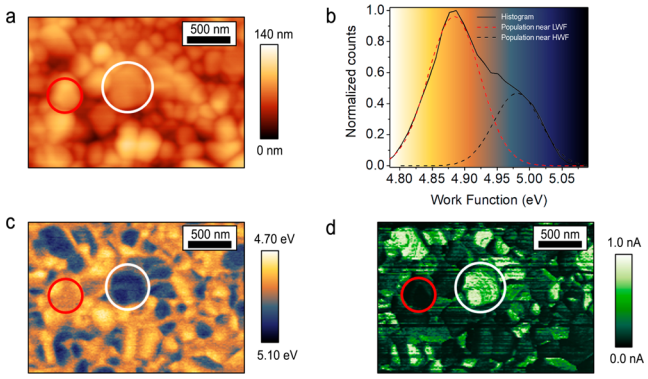

Figure 2. SPM images of MAPI-$PbAc_2$ deposited on a glass/ITO/PEDOT:PSS substrate showing the (a) topography, (b) work function histogram (with the color grading used in (c)), (c) work function (measured with FM-KPFM), and (d) current image (measured with C-AFM in the peak-force tunneling TUNA mode, with an applied dc sample bias of 1.7 V). Note that the FM-KPFM and C-AFM measurements were carried out at the same location. Colored circles highlight HWF domains (white circle) and LWF domains (red circle).

see experimental details). Figure 2c shows spatial heterogeneity of the WF at the surface of the film, as highlighted by the complex WF distribution curve in Figure 2b. Note that the surface properties are studied at the MAPI/N_2 interface; however, there may be substantial changes on the interface properties when the contact with $MAPbI_3$ is made with other gas (like oxygen) or films used for device applications. The substrate on which the perovskite is grown and/or the operating conditions (*i.e.*, temperature or pressure) may also affect the surface properties. The WF distribution can be deconvoluted into two dominating populations, which have an average difference of 0.1 eV. The high WF (HWF) domain and the low WF (LWF) domain are highlighted by white and red circles in Figure 2c, respectively. Results will be discussed as if there were two clearly distinguished populations, although since the deconvoluted profiles are quite large and overlap, there might be intermediate populations lying between and outside the dominating contributions. Those two domains show up to 0.2 eV WF difference and have average WF values of 4.8 and 5.0 eV for LWF and HWF, respectively. The schematic representations of LWF, HWF, and on the KPFM configuration can be seen in Figure S1.

The measured WF values lie in a range between 4.70 and 5.10 eV. The reported electron affinity and ionization energy for $MAPbI_3$ are most commonly around 3.9 and 5.4 eV, respectively, although there is some scatter in the literature.[46−49] This would indicate that despite the heterogeneous WF at the surface of the film, the Fermi level remains located between the valence band edge and midgap, *i.e.*, the whole surface of the MAPI-$PbAc_2$ thin film is exhibiting a p-type semiconducting behavior and hence with holes as majority carriers.[46] Notice that the topographic profile does not influence or correlate with the CPD signal (see Figure S2a); in other words, the contrast in WF images only arises from the electrostatic probing and is, in no manner, due to topographical variations of the surface.

Next, C-AFM was performed at the same location. Upon positive dc sample bias, holes are injected from the ITO/PEDOT:PSS bottom electrode into the valence band of the MAPI-$PbAc_2$ and transported across the film prior to collection at the tip−sample contact. Likewise for FM-KPFM measurements, a spatially heterogeneous current response is observed, as shown in Figure 2d. A correlation clearly appears, with the HWF (LWF) domains corresponding to high (low) current domains, as exemplified by the white (red) circles in Figure 2c,d, respectively. This correlation between current and WF is further evidenced by the averaged scatter plot shown in Figure S2c. The current variation with topography was meanwhile found to be inside the error bar when compared to the height variations (see Figure S2b), indicating little if no correlation also between these two signals.

Because FM-KPFM is probing surface properties, the observed correlation between FM-KPFM and C-AFM images strongly supports that the C-AFM response is also related to the perovskite surface properties. In other words, the C-AFM current is ruled by perovskite surface properties (*i.e.*, the local work function) at the tip−sample contact.

So far, we observed two different surface domains associated with given local work functions and, at the same time, we found them to be related to different current densities.

Surface heterogeneity is further investigated by means of averaged C-AFM images taken at different biases, where $I-V$ profiles are built for different domains. Figure 3a displays the C-AFM current variations with bias at these two locations, exhibiting an exponential law between 1 and 2 V in both domains, consistent with a specific injection/extraction dominating mechanism. In this bias range, the $I-V$ profiles are characteristic of that of a rectifying diode, suggesting for both locations a Schottky-like contact at the tip−sample contact with an associated built-in potential (V_{bi}) in the films. MAPI-$PbAc_2$ exhibits a p-type behavior; this diode-like contact is therefore biased in forward polarity upon positive dc sample bias.

For a standard Schottky contact, the charge transport between the probe and the sample in forward bias is

https://dx.doi.org/10.1021/acsanm.0c01687
ACS Appl. Nano Mater. 2020, 3, 8268−8277

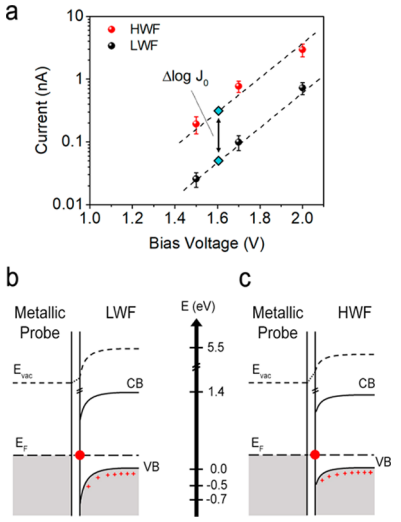

Figure 3. (a) Semilog plot of the bias dependence of the C-AFM current (measured in the contact mode) for the LWF and HWF types of $MAPbI_3$ domains. (b) and (c) Scheme of the C-AFM band structure of the probe−surface contact for the two types of domains, LWF and HWF, at 0 V. The surface states (represented by the red dot) impact the position of the Fermi level at the $MAPbI_3$ surface. There is an interface layer between LWF/HWF and the metallic probe, which allows for vacuum-level adjustment.

conditioned by the thermionic emission theory, whose analytical expression is

$$J = J_0\, e^{qV/nkT}\,(1 - e^{-qV/kT}) \quad (1)$$

where J is the current density, J_0 is the saturation current density obtained in reverse bias, q is the charge of an electron, V is the voltage applied to the sample, n is the ideality factor of the diode, k is the Boltzmann constant, and T is the temperature,[50] with $J_0 \propto e^{-q\phi_b/kT}$, where ϕ_b is the effective barrier of the Schottky contact. The ideality factors, determined from the slope in the semilog profiles of Figure 3a, are similar. The difference in current between the two types of domains in the semilog $I-V$ curve can therefore be mainly attributed to different effective barriers ($\Delta\phi_b$). Figure 3b,c illustrates this case scenario, where holes must overcome a higher barrier in LWF domains before they can be collected by the metallic probe.

The effective barriers (ϕ_b) were experimentally extracted from Figure 3a and are ∼0.45 and ∼0.70 eV for HWF and LWF, respectively. If we consider the measured barrier heights and compare them to the measured WF, the valence band (VB) is found to lie at ∼5.5 eV for both types of domains. An optical band gap of 1.59 eV was experimentally determined by UV−visible absorption spectroscopy; see Figure S3. Even if the perovskite films have domains with heterogeneous surface properties, local photoluminescence studies have shown similar emission wavelengths for different domains, *i.e.*, similar band

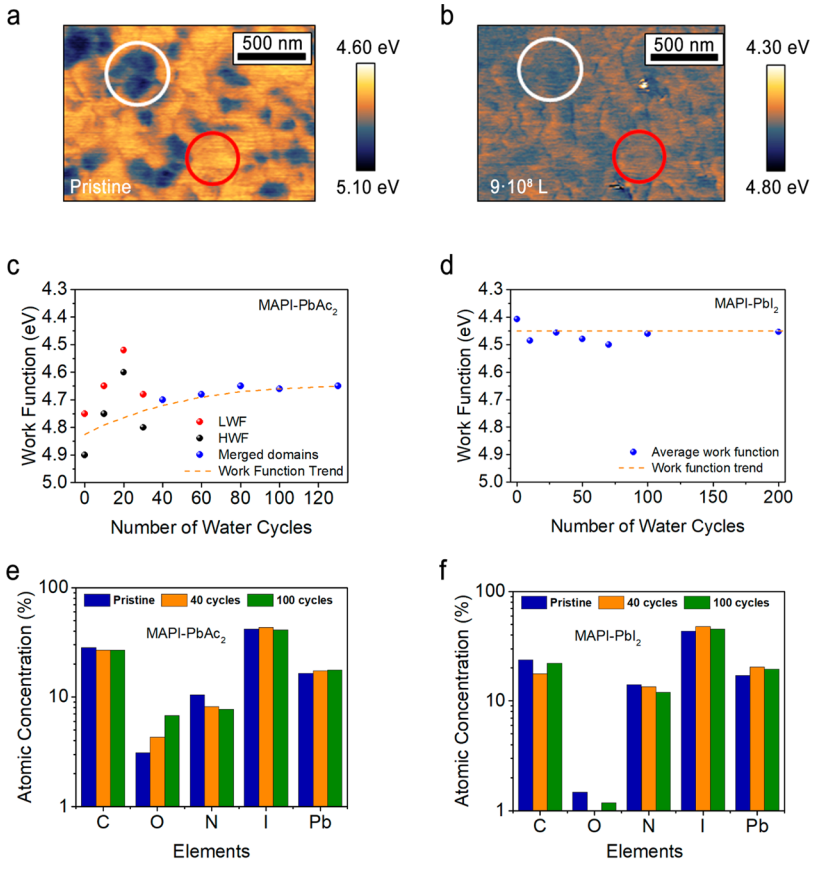

Figure 4. Work function images of the MAPI-$PbAc_2$ (a) pristine film and (b) after exposure to 100 cycles of water vapor. Graph (c) shows the WF evolution of MAPI-$PbAc_2$, while graph (d) shows the WF evolution for MAPI-PbI_2 upon water exposure. Graphs (e) and (f) represent the atomic concentrations measured by XPS for MAPI-$PbAc_2$ and MAPI-PbI_2, respectively. Merged domains (blue dots in (c) and (d)) stand for the situations where domains can no longer be distinguished so only the average WF value of the sample is considered.

https://dx.doi.org/10.1021/acsanm.0c01687
ACS Appl. Nano Mater. 2020, 3, 8268−8277

gaps.[51] Therefore, even if the perovskite film shows heterogeneous WF at the surface, we consider that the optical band gap remains constant at the surface. The band-gap value obtained is in close vicinity to what is traditionally reported in the literature and can be used to determine the position of the conduction band (CB) at the surface ~3.9 eV.[46] The variations of WF and ϕ_b between HWF and LWF domains are also consistent with the p-type semiconducting character of $MAPbI_3$, with lower (higher) WF inducing higher (lower) ϕ_b. Generally, the WF and free carrier density (p) are conditioned by the sole crystallinity of the film and play a primary role in charge collection, determining the injection voltages.[52,53] In this work, however, charge injection/extraction mechanisms dominate the current response up to much higher injection voltages, indicating a significant amount and impact of surface states, hence leading to possible interfacial issues once incorporated in devices.[54,55] This is likely to induce a Fermi-level pinning located at the energy level of the traps (4.8 and 5.0 eV as previously shown). In C-AFM, the alignment of the Fermi level takes place between the probe and the sample in both LWF and HWF domains with their respective trap energy levels at 0 V. This Fermi-level pinning has an impact on the probe−sample contact and can be described with an additional electric field across an interfacial layer as depicted in Figure 3b,c.

The existence of domains exhibiting different surface states despite similar stoichiometry can be attributed to, at least, two kinds of different perturbing states; they could either be the result of different terminations or be the result of the growth procedure. Recent DFT calculations gave insights into the effect of the possible different $MAPbI_3$ terminations.[56] Pure methylammonium(MAI)-terminated (001) surfaces are around 1 eV higher in energy than pure PbI_2-terminated (001) surfaces, both independently affecting the charge injection properties.[57,58] In addition, MAI-terminated surfaces are expected to have a higher band gap than PbI_2-terminated surfaces.[58] However, given the fact that the two types of domains observed here exhibit similar VB, it is quite unlikely that they would correspond to two different surface terminations. We are therefore led to hypothesize that surface structural defects induced by the growth conditions would cause the observed local electronic heterogeneity. However, at this point, we cannot completely discriminate between these two possibilities.

2.2. Degradation Process. The stability of perovskite films is usually addressed either for the whole solar cell device or for the perovskite layer itself.[9] The perovskite device or film is typically exposed to different humidity levels or to ambient conditions. In this section, we develop a more controlled approach for exposing the perovskite films to very small amounts of water vapor. First, the perovskite films were introduced in a low-vacuum chamber (~1.15 torr) with 0.88 dm^3 volume. Water vapor was then injected by cycles into the chamber, heated at ~55 °C, and purged by a continuous nitrogen flow to hinder any condensation. Each cycle corresponds to a pulse of water and then flushing it away before the next one. This method allows a very precise control of the water quantity to which the sample is exposed. For comparison, Li et al. reported a threshold of 2×10^{10} L (1 L corresponds to 10^{-6} torr·s^{-1}) for the $MAPbI_3$ to decompose, based on XPS measurements.[59] In this work, the samples were exposed to much lower amounts of water, *i.e.*, from 2.25×10^8 L up to 5×10^9 L, which allows one to follow earlier stages of the degradation process. Then, the WF was measured with KPFM, taking care to always probe the same location (Figure 4a,b). Upon exposure to water, the WF of the MAPI-$PbAc_2$ surface tends to decrease for both types of domains (HWF and LWF) toward a common value, as shown in Figure 4c. After 9×10^8 L (40 cycles) of water exposure, HWF and LWF domains can no longer be distinguished, and, upon further water exposure, the WF tends to stabilize ~4.6 eV. Note that at such low exposure, the topographic profile remains unchanged (Figure S7a). The final WF value corresponds to the Fermi level being in the vicinity of the midgap. For a nonperfect crystal, such an intrinsic behavior (having the Fermi level at midgap) can only be attributed to semi-insulating properties, where the energy bands are depopulated from their free carriers by deep traps, inducing a weak conduction. This makes the perovskite behave as an insulator. The fact that the WF values are moving toward the midgap upon water exposure for both domains excludes the previous hypothesis of different surface terminations. PbI-terminated surfaces are more resistant to water interactions compared to MAI-terminated surfaces,[60] which would result in a delayed WF shift toward midgap values. Instead, in a perovskite system with defects, the position of the Fermi level at midgap rather relates to the formation of deep traps. Consistently, no C-AFM current could be detected after more than 10 cycles of water exposure. Therefore, there is a distribution of surface states on the MAPI-$PbAc_2$ surface that induces a difference in the carrier injection/extraction previously shown in Figure 3a. Such a heterogeneous surface can potentially lower not only the performance of the device but also its stability.

These observations are comparable to the previously reported study by Ralaiarisoa et al. where a perovskite film was exposed to $\sim 2 \times 10^4$ L, showing a reversible water adsorption.[61] Higher exposures, $\sim 1 \times 10^{10}$ L, resulted in a WF decrease of 0.33 eV, attributed to an increase of Pb^0-related surface states. The present work studies the water interaction in the upper exposure range of the previous study.

These results indicate that for the MAPI-$PbAc_2$ films, very small exposure to water is enough to strongly affect the electronic properties by creating deep trap states, hence suppressing the charge transport. In this scenario, in a pristine p-type perovskite, the presence of surface states makes the surface less p-type, as schematically shown in Figure 3b,c, and the possible point defects to be considered are donor sites lying above the Fermi level. These defects can be induced by I vacancies (V_I), substitution of Pb and MA cations at I sites (Pb_I and MA_I, respectively), substitution of Pb ions at MA sites (Pb_{MA}), and MA and Pb interstitials (MA_i and Pb_i, respectively).[36] Among these defects, we consider MA_i, and V_I to potentially dominate due to their lower formation energies.[62,63]

We also investigated the effect of water exposure on the perovskite prepared from the PbI_2 precursor (MAPI-PbI_2). The resulting $MAPbI_3$ thin films can be self-doped depending on the ratio between the precursors used in the synthesis process.[64] High (low) concentrations of PbI_2 in the precursor solution make the final perovskite film more n-type (p-type, respectively). Moreover, PEDOT:PSS has a better affinity to PbI_2 than to MAI, so even higher amounts of MAI are necessary to generate a p-type $MAPbI_3$ perovskite on the PEDOT:PSS surface.[65] Above, we used MAPI-$PbAc_2$, the synthesis of which results in a p-type material. To prepare an n-type perovskite, we used PbI_2 as the precursor in a 1:1 (PbI_2/

https://dx.doi.org/10.1021/acsanm.0c01687
ACS Appl. Nano Mater. 2020, 3, 8268−8277

MAI) ratio, so we would expect a favored n-type character during the synthesis process. It corresponds to one of the most typical synthesis routes used in $MAPbI_3$ perovskite solar cells.[66−69]

The MAPI-PbI_2 perovskite surface in this case shows a narrow WF distribution; see Figure S4d. Consistently, the C-AFM current distribution shows only one major peak (Figure S4e); the small peak at zero current corresponds to insulating PbI_2 domains (highlighted in Figure S4c) and is confirmed by the small peak at 12.6° in the XRD diffractogram (Figure 5c).

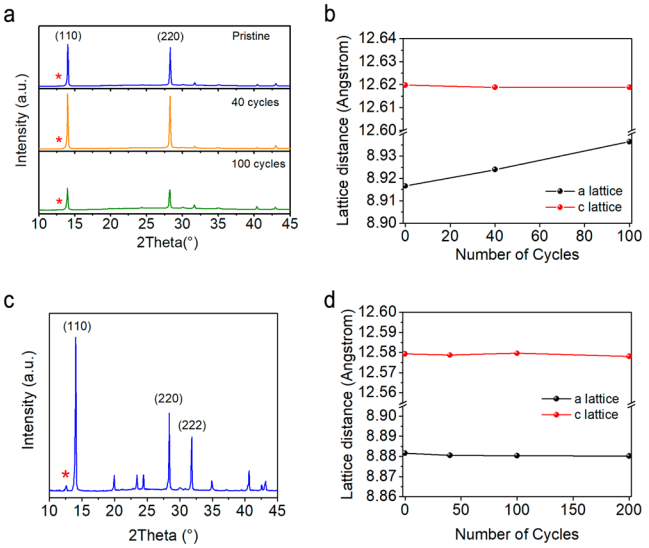

Figure 5. (a) XRD diffractograms of the MAPI-$PbAc_2$ pristine and water-exposed (b) MAPI-$PbAc_2$ lattice distance displacement upon water vapor exposure. (c) XRD diffractogram of the MAPI-PbI_2 pristine sample and (d) MAPI-PbI_2 lattice distance displacement upon water vapor exposure. Lattice *a* (*c*) stands for the shorter (longer) axis in the tetragonal structure.

As observed in Figure 4d (and Figure S4b), the WF of the MAPI-PbI_2 lies around 4.4 eV. The band-gap energy is ∼1.56 eV (Figure S3b), in line with the band gap reported in the literature.[3] Based on (i) our experimental protocol and (ii) what is regularly and consistently reported in the literature, we assume these MAPI-PbI_2 films to exhibit n-type semiconducting properties.

When exposing the MAPI-PbI_2 surface to pulsed water vapor cycles, the WF remains unchanged up to 200 cycles (Figure 4d). The C-AFM current also remains constant up to 200 cycles (see Figure S5). This is in strong contrast to the MAPI-$PbAc_2$ material, for which no current could be measured after the first 10 water vapor cycles (corresponding to 2.25×10^8 L). Comparing further MAPI-PbI_2 with MAPI-$PbAc_2$, and with a work function located closer to the midgap than to the conduction band, the trap states observed on the MAPI-PbI_2 surface are expected to be acceptor ones inducing deep states. These surface acceptor defects seem to be less reactive upon water exposure; therefore, we assume n-type surfaces such as MAPI-PbI_2 are more stable at the early stage of water-induced degradation.

Both pristine $MAPbI_3$ materials were also characterized by XPS, and similar measurements were carried out after exposure to 40 and 100 water vapor cycles. Figure 4e shows the variations of the atomic concentration of the elements forming the MAPI-$PbAc_2$ films. Upon exposure to water, a significant increase in the oxygen content at the surface can be observed and, simultaneously, a decrease in the nitrogen concentration. In contrast, the nitrogen concentration barely changes in MAPI-PbI_2 upon water exposure, while no significant amount of oxygen is observed (Figure 4f). It is tempting to relate these behaviors to the WF shift toward the midgap observed in water-exposed MAPI-$PbAc_2$ films (Figure 4c) and the constant WF value for MAPI-PbI_2 films (Figure 4d). The Pb:I elemental ratio for both materials (1:3) remains constant even after exposure to 100 cycles of water vapor, indicating that a possible degradation cannot be attributed here to perovskite segregation at the surface and thus a change in stoichiometry. Interestingly, the traps expected to be present on the MAPI-$PbAc_2$ surface, V_I and MA_i, are typically positively charged, which would imply that they are keen to interact with the electronegative oxygen atoms from water molecules. As for MAPI-PbI_2, the considered defects, V_{Pb} and I_i, are negatively charged, which would make them more difficult for the oxygen to interact.

The water−perovskite interaction is further confirmed by the XRD measurements carried out after similar amounts of cycles of exposure to water vapor shown in Figure 5a for MAPI-$PbAc_2$ and Figure S6 for MAPI-PbI_2. The main XRD peaks in MAPI-$PbAc_2$ are located at 14.04 and 28.31°, corresponding to the X-ray scattering from the (110) and (220) planes; Figure 5a.[3] After exposing the MAPI-$PbAc_2$ sample to 100 cycles of water, there is a reduction in the X-ray scattering intensities while the characteristic PbI_2 signal is not present, indicating that the perovskite did not start structural degradation yet. On the other hand, in the MAPI-PbI_2 film, apart from the most intense peaks at 14.07 and 28.40°, there is another intense peak at 31.82° attributed to the (222) plane; Figure 5c. The low-intensity feature at 12.65° in the XRD diffractogram for MAPI-PbI_2 indicates the presence of unreacted PbI_2.[45] The reduction in intensity of the XRD features seen for MAPI-$PbAc_2$ could be related to the change in morphology observed with AFM (Figure S7b). Figure S7c shows the variations of the morphology of the MAPI-$PbAc_2$ layer upon exposure to water vapor, as described by the power density spectrum of the AFM images. The gradual increase of the spectral density at high wavenumbers (*i.e.*, smaller spatial distances) for MAPI-$PbAc_2$ indicates that the relative amount of small grains increases when increasing the water exposure. This is illustrated by the image in Figure S7b, which shows the surface morphology after 150 cycles of water exposure (which corresponds to amounts of water similar to that reported in the literature). The large grains initially present have broken up into smaller features, which is expected to strongly impact the electronic properties, as amply reported in the literature.[59] It is also important to notice that the spectral density of the MAPI-PbI_2 material is much less sensitive to water exposure (Figure S7d), consistent with the better preservation of the electronic properties.

The highest XRD intensity peak in both $MAPbI_3$ films is the (110) peak, and it is used to measure the *a* lattice constant, which corresponds to the short lattice distance in a tetragonal geometry. The long lattice distance, the c lattice, is calculated mainly from the (222) peak. As a result, Figure 5b,d shows the evolution of the *a* and *c* lattice distances upon water exposure in MAPI-$PbAc_2$ and MAPI-$PbAc_2$, respectively. For MAPI-$PbAc_2$, only the *a* lattice parameter is increased when exposing the sample to water. This lattice expansion could be related to a reaction between the MA^+ cation and water molecules, which

https://dx.doi.org/10.1021/acsanm.0c01687
ACS Appl. Nano Mater. 2020, 3, 8268−8277

has been proposed by Li et al. This is discussed below on the basis of the XPS results and is consistent with the positively charged defects reacting with water.[59] In contrast, in MAPI-PbI_2, both lattice distances remain constant up to 200 cycles of water exposure (Figure 5d).

To elucidate the specific interactions of water with MAPI-$PbAc_2$ and MAPI-PbI_2, we recorded high-resolution XPS core-level spectra. The C 1s core-level spectrum of MAPI-$PbAc_2$ shows two clear peaks at 285.1 and 286.8 eV, for C−C and C−N groups, respectively; Figure 6a.[70] After 40 and 100 cycles of water, the C 1s photoemission peaks and the relative carbon concentration remain unchanged, as observed in Figures 6c,e, and 4e. Since the nitrogen content was shown to decrease after water exposure along with the increase of the oxygen content, the peak at 286.8 eV for MAPI-$PbAc_2$ can be attributed to a combination of contributions from C−N groups and C−O groups. The evolution of the oxygen and nitrogen contents is consistent with the occurrence of a nucleophilic substitution reaction by which the oxygen atom of a water molecule binds to the carbon atom of methylammonium, expelling one ammonia molecule that is pumped away. Although this reaction is kinetically not favorable, we think that it is enhanced by the vacuum chamber heat (~55 °C). This chemical reaction is expected to deeply affect the electronic properties of the materials. Note however that the increase in the oxygen content is much stronger than the decrease in the nitrogen content (Figure 4e), which suggests that part of the water molecules simply adsorbs on MAPI-$PbAc_2$ (and could further modify its electronic properties *via* electrostatic interactions).

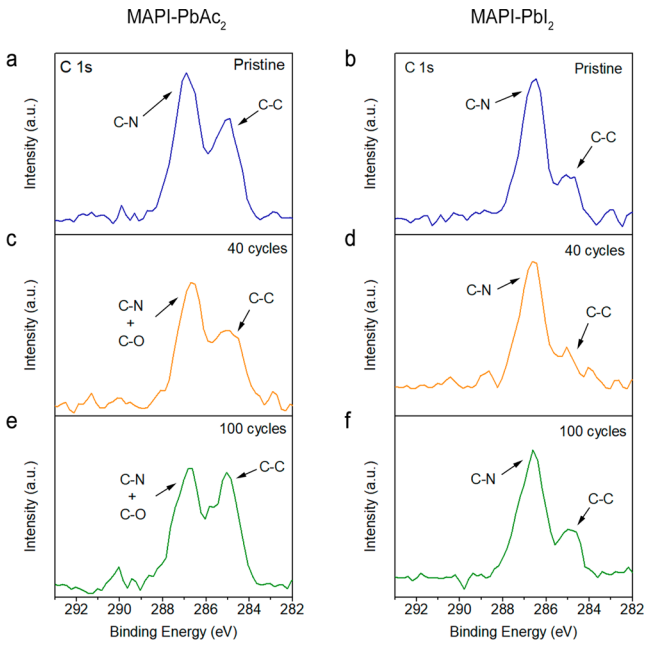

Figure 6. C 1s core-level XPS spectra of MAPI-$PbAc_2$ (a, c, e) and MAPI-PbI_2 (b, d, f): pristine (a, b), exposed to 40 cycles (c, d) and to 100 cycles of water (e, f).

The C 1s core-level spectrum of the MAPI-PbI_2 shows two peaks at ~ 285 eV and ~ 287 eV, similar to the MAPI-$PbAc_2$ peaks. However, not only the C 1s peaks and the relative concentration of carbon remain unaffected but also the concentration of oxygen and nitrogen remains unchanged upon water exposure, as shown in Figures 6b,d,f, and 4f. This observation confirms that MAPI-PbI_2 is less reactive with water.[71] The binding energies for the nitrogen, oxygen, lead, and iodine core levels do not change even after 100 water cycles; Figure S8.

3. CONCLUSIONS

In this work, we combined FM-KPFM and C-AFM to study locally the electronic properties of the $MAPbI_3$ perovskite surface, for materials obtained *via* two different synthetic routes. When using the lead acetate precursor, we evidenced local variations (by up to 0.2 eV) in the WF values, with HWF regions corresponding to higher current values. LWF regions with surface states closer to the midgap are shown to further hinder carrier injection/extraction at the surface and hence the charge transport in the film. In contrast, when using the lead iodide precursor, the WF distribution over the surface appears much more homogeneous. We interpret these measurements as indicative of different types of defects on the perovskite surface. We suggest that MA_i and V_I are present on the MAPI-$PbAc_2$ surfaces and, therefore, on most of the p-type $MAPbI_3$ perovskites. In the same manner, MAPI-PbI_2 surfaces, and therefore most of the n-type $MAPbI_3$ perovskites, have donor defects.

In a second stage, we have attempted to relate the electronic structures at the surface of the $MAPbI_3$ with their stability upon water vapor exposure. In MAPI-$PbAc_2$, the WF decreases after water exposure. This was shown to correspond to a drift of the Fermi level toward the midgap, indicating the creation of deeper trap states turning the perovskite into a semi-insulator, consistent with the collapse of the current signal. The XPS measurements indicate that the methylammonium groups are likely to react with water molecules releasing NH_3 and creating C−O bonds. Higher stability against moisture was observed for MAPI-PbI_2. This was attributed to the different nature of defects, acceptors compared to donors. By using a methodology that allows a precise control in exposure to very small amounts of water, we could study early degradation mechanisms in perovskites at the nanoscale. We observed that strong interaction with water molecules can occur very quickly in p-type perovskites like MAPI-$PbAc_2$. This rapid interaction with water alters the electronic and transport properties even prior to any morphological or stoichiometric changes, which can result in a degraded photovoltaic cell.

4. METHODS

4.1. Device Fabrication. The cleaning process of patterned indium tin oxide (ITO) substrates (Naranjo substrates, ref NS1463, 95 nm, ~20 Ω.sq) includes the successive steps: wiping with RBS, followed by 10 min of ultrasonication in deionized water, acetone, and isopropanol, and drying by pure N_2 flow. Prior to deposition, the substrates were exposed to O_2 plasma in primary vacuum for 5 min. PEDOT:PSS (Heraeus Clevios P Al 4083) was then spin-coated at 5000 rpm for 60 s and annealed at 110 °C for 10 min to remove water traces before introduction into the inert atmosphere environment, *i.e.*, a N_2-filled glovebox. The perovskite synthesis and deposition were carried out in two different ways, and the corresponding materials are referred to as MAPI-$PbAc_2$ and MAPI-PbI_2. MAPI-$PbAc_2$ was obtained by mixing methylammonium iodide MAI (Greatcell Solar) and lead acetate trihydrate ($PbAc_2{\cdot}3H_2O$) (99.999% Merck) into anhydrous *N*,*N*-dimethylformamide (DMF, 99.9% Merck) at a 3:1 molar ratio with a final concentration of 0.5 M. Hydrophosphorous acid (50% Merck) was added with an HPA/$PbAc_2{\cdot}3H_2O$ molar ratio of 11%.[41,42] The solution was then spin-coated at 2000 rpm for 60 s, left at room temperature for 10 min, and heated at 100 °C for 5 min.

https://dx.doi.org/10.1021/acsanm.0c01687
ACS Appl. Nano Mater. 2020, 3, 8268−8277

The MAPI-PbI_2 perovskite was prepared by mixing lead iodide PbI_2 (99% Merck) and MAI in DMF and dimethyl sulfoxide (DMSO) at a concentration of 1.5 M. The solution was spin-coated at 5000 rpm for 30 s, while 200 μL of ethyl acetate was dropped into the spinning sample after 10 s to control the end point of the growth procedure.[68,69] Both routes lead to perovskite film thickness of ~300 nm.

4.2. Perovskite Characterization. Perovskite thin films were characterized in an inert atmosphere (N_2-filled glovebox) by means of a Multimode 8 Atomic Force Microscope (Bruker) equipped with a Nanoscope V controller and coupled to a NANONIS (by Specs) external controller for FM-KPFM measurements. All of the measurements performed in this work by AFM were done in dark conditions.

In FM-KPFM, the surface potential measurement is based on an electrostatic force gradient detection, rather than on a direct force detection. This conditions the measured signal to the probe apex, hence guaranteeing high spatial resolution (<50 nm).[25−30] Since FM-KPFM allows the determination of surface potential by measuring the WF difference between the tip and the sample (CPD), preliminary determination of the tip WF on a reference sample is required to derive that of the sample under test. This is done by recording the CPD on a highly ordered pyrolytic graphite surface (WF of 4.65 eV).[72] PPP-EFM (Nanosensors GmbH) metal-coated ($PtIr_5$) etched Si probes were operated at the excitation frequency of ~75 kHz, corresponding to the first resonance of the cantilever. FM-KPFM operated the modulated probe 15−20 nm above the sample surface and with an excitation amplitude of ~10 nm, rastering the sample at a scan rate of 0.3 Hz.

Current measurements were carried out in the contact mode for the $I-V$ curves and in the peak-force tapping TUNA (PF-AFM) mode for image acquisition. In PF-AFM, the eponymous external module (Bruker) is coupled to the multimode microscope. PF-TUNA is an intermittent contact AFM method operating at 2 kHz, with force control in the nano-Newton range, likely to avoid induced damage to the sample. The external controller is equipped with two current amplifiers, allowing current detection down to 100 fA. Current across the tip−sample system is obtained by dc biasing the sample *vs* the grounded tip.[73] SCM-PIT metal-coated (PtIr) conductive probes (Bruker) with a spring constant of ~3 N/m were used. PF-TUNA operated at a scan rate of 0.3 Hz with a force setpoint of 4 nN and an amplitude of oscillation of 50 nm.

The X-ray diffractograms were obtained using a Panalytical Empyrean XRD diffractometer operating with the Cu $K_{\alpha 1}$ (α = 0.1542 nm) source. The XPS measurements were carried out with a PHI 5300ESCA Perkin-Elmer spectrometer, and the spectra were calibrated with the C 1s peak (285.1 eV). The water exposure of the perovskite samples was done in a vacuum chamber at 1.15 torr average pressure. Water was injected into the chamber by cycles, where each cycle corresponds to a pulse of water and flushing it away with nitrogen gas. Considering that each cycle lasts 15 s and that 1 L corresponds to 10^{-6} torr·s^{-1}, we estimated the exposure to be 5×10^9 L for 200 cycles.

■ ASSOCIATED CONTENT

Supporting Information

The Supporting Information is available free of charge at https://pubs.acs.org/doi/10.1021/acsanm.0c01687.

KPFM and C-AFM crosstalk; UV−visible absorption with the corresponding optical band gap; MAPI-PbI_2 SPM images; statistical data from AFM images; XRD diffractograms; XPS core-level information (PDF)

■ AUTHOR INFORMATION

Corresponding Author

Philippe Leclère − *Laboratory for Chemistry of Novel Materials, Materials Research Institute, University of Mons, B-7000 Mons, Belgium;* orcid.org/0000-0002-5490-0608; Email: Philippe.leclere@umons.ac.be

Authors

Jaume Llacer − *Laboratory for Chemistry of Novel Materials, Materials Research Institute, University of Mons, B-7000 Mons, Belgium; Institute of Electronics, Microelectronics and Nanotechnology, University of Lille, F-59652 Villeneuve d'Ascq Cedex, France*

David Moerman − *Materia Nova R&D Center, B-7000 Mons, Belgium*

Olivier Douhéret − *Materia Nova R&D Center, B-7000 Mons, Belgium*

Xavier Noirfalise − *Materia Nova R&D Center, B-7000 Mons, Belgium*

Claudio Quarti − *Laboratory for Chemistry of Novel Materials, Materials Research Institute, University of Mons, B-7000 Mons, Belgium;* orcid.org/0000-0002-5488-1216

Roberto Lazzaroni − *Laboratory for Chemistry of Novel Materials, Materials Research Institute, University of Mons, B-7000 Mons, Belgium; Materia Nova R&D Center, B-7000 Mons, Belgium;* orcid.org/0000-0002-6334-4068

Didier Théron − *Institute of Electronics, Microelectronics and Nanotechnology, University of Lille, F-59652 Villeneuve d'Ascq Cedex, France*

Complete contact information is available at: https://pubs.acs.org/10.1021/acsanm.0c01687

Notes

The authors declare no competing financial interest.

■ ACKNOWLEDGMENTS

This work was supported by the University of Lille and the University of Mons through a joint doctoral fellowship (J.L.). The research in Mons was also supported by FNRS *via* the "Consortium des Equipements de Calcul Intensif" (CECI) program and the Excellence of Science "2Dto3D" project. P.L. is Senior Research Associate of FRS-FNRS (Belgium). The work in Materia Nova was supported by the European Union's Horizon 2020 Research and Innovation Program under Grant Agreement No. 761036 (MAMMA project).

■ REFERENCES

(1) Kojima, A.; Teshima, K.; Shirai, Y.; Miyasaka, T. Organometal Halide Perovskites as Visible-Light Sensitizers for Photovoltaic Cells. *J. Am. Chem. Soc.* **2009**, *131*, 6050−6051.

(2) Jiang, Q.; Zhao, Y.; Zhang, X.; Yang, X.; Chen, Y.; Chu, Z.; Ye, Q.; Li, X.; Yin, Z.; You, J. Surface Passivation of Perovskite Film for Efficient Solar Cells. *Nat. Photonics* **2019**, *13*, 460−466.

(3) Lee, M. M.; Teuscher, J.; Miyasaka, T.; Murakami, T. N.; Snaith, H. J. Efficient Hybrid Solar Cells Based on Meso-Superstructured Organometal Halide Perovskites. *Science* **2012**, *338*, 643−647.

(4) Wehrenfennig, C.; Eperon, G. E.; Johnston, M. B.; Snaith, H. J.; Herz, L. M. High Charge Carrier Mobilities and Lifetimes in Organolead Trihalide Perovskites. *Adv. Mater.* **2014**, *26*, 1584−1589.

(5) Zhumekenov, A. A.; Saidaminov, M. I.; Haque, M. A.; Alarousu, E.; Sarmah, S. P.; Murali, B.; Dursun, I.; Miao, X.-H.; Abdelhady, A. L.; Wu, T.; Mohammed, O. F.; Bakr, O. M. Formamidinium Lead Halide Perovskite Crystals with Unprecedented Long Carrier Dynamics and Diffusion Length. *ACS Energy Lett.* **2016**, *1*, 32−37.

(6) Tian, W.; Zhao, C.; Leng, J.; Cui, R.; Jin, S. Visualizing Carrier Diffusion in Individual Single-Crystal Organolead Halide Perovskite Nanowires and Nanoplates. *J. Am. Chem. Soc.* **2015**, *137*, 12458−12461.

(7) Miyata, K.; Meggiolaro, D.; Trinh, M. T.; Joshi, P. P.; Mosconi, E.; Jones, S. C.; Angelis, F. D.; Zhu, X.-Y. Large Polarons in Lead Halide Perovskites. *Sci. Adv.* **2017**, *3*, No. e1701217.
(8) Batignani, G.; Fumero, G.; Srimath Kandada, A. R.; Cerullo, G.; Gandini, M.; Ferrante, C.; Petrozza, A.; Scopigno, T. Probing Femtosecond Lattice Displacement upon Photo-Carrier Generation in Lead Halide Perovskite. *Nat. Commun.* **2018**, *9*, No. 1971.
(9) Wang, R.; Mujahid, M.; Duan, Y.; Wang, Z.-K.; Xue, J.; Yang, Y. A Review of Perovskites Solar Cell Stability. *Adv. Funct. Mater.* **2019**, *29*, No. 1808843.
(10) Mesquita, I.; Andrade, L.; Mendes, A. Perovskite Solar Cells: Materials, Configurations and Stability. *Renewable Sustainable Energy Rev.* **2018**, *82*, 2471−2489.
(11) Yun, J. S.; Seidel, J.; Kim, J.; Soufiani, A. M.; Huang, S.; Lau, J.; Jeon, N. J.; Seok, S. I.; Green, M. A.; Ho-Baillie, A. Critical Role of Grain Boundaries for Ion Migration in Formamidinium and Methylammonium Lead Halide Perovskite Solar Cells. *Adv. Energy Mater.* **2016**, *6*, No. 1600330.
(12) Shao, Y.; Fang, Y.; Li, T.; Wang, Q.; Dong, Q.; Deng, Y.; Yuan, Y.; Wei, H.; Wang, M.; Gruverman, A.; Shield, J.; Huang, J. Grain Boundary Dominated Ion Migration in Polycrystalline Organic−Inorganic Halide Perovskite Films. *Energy Environ. Sci.* **2016**, *9*, 1752−1759.
(13) Du, M.-H. Density Functional Calculations of Native Defects in CH3NH3PbI3: Effects of Spin−Orbit Coupling and Self-Interaction Error. *J. Phys. Chem. Lett.* **2015**, *6*, 1461−1466.
(14) Chen, B.; Yang, M.; Priya, S.; Zhu, K. Origin of J−V Hysteresis in Perovskite Solar Cells. *J. Phys. Chem. Lett.* **2016**, *7*, 905−917.
(15) Kong, W.; Ding, T.; Bi, G.; Wu, H. Optical Characterizations of the Surface States in Hybrid Lead−Halide Perovskites. *Phys. Chem. Chem. Phys.* **2016**, *18*, 12626−12632.
(16) Snaith, H. J.; Abate, A.; Ball, J. M.; Eperon, G. E.; Leijtens, T.; Noel, N. K.; Stranks, S. D.; Wang, J. T.-W.; Wojciechowski, K.; Zhang, W. Anomalous Hysteresis in Perovskite Solar Cells. *J. Phys. Chem. Lett.* **2014**, *5*, 1511−1515.
(17) Wu, X.; Trinh, M. T.; Niesner, D.; Zhu, H.; Norman, Z.; Owen, J. S.; Yaffe, O.; Kudisch, B. J.; Zhu, X.-Y. Trap States in Lead Iodide Perovskites. *J. Am. Chem. Soc.* **2015**, *137*, 2089−2096.
(18) Xiao, Z.; Bi, C.; Shao, Y.; Dong, Q.; Wang, Q.; Yuan, Y.; Wang, C.; Gao, Y.; Huang, J. Efficient, High Yield Perovskite Photovoltaic Devices Grown by Interdiffusion of Solution-Processed Precursor Stacking Layers. *Energy Environ. Sci.* **2014**, *7*, 2619−2623.
(19) Shi, D.; Adinolfi, V.; Comin, R.; Yuan, M.; Alarousu, E.; Buin, A.; Chen, Y.; Hoogland, S.; Rothenberger, A.; Katsiev, K.; Losovyj, Y.; Zhang, X.; Dowben, P. A.; Mohammed, O. F.; Sargent, E. H.; Bakr, O. M. Solar Cells. Low Trap-State Density and Long Carrier Diffusion in Organolead Trihalide Perovskite Single Crystals. *Science* **2015**, *347*, 519−522.
(20) Buin, A.; Pietsch, P.; Xu, J.; Voznyy, O.; Ip, A. H.; Comin, R.; Sargent, E. H. Materials Processing Routes to Trap-Free Halide Perovskites. *Nano Lett.* **2014**, *14*, 6281−6286.
(21) Nie, W.; Tsai, H.; Asadpour, R.; Blancon, J.-C.; Neukirch, A. J.; Gupta, G.; Crochet, J. J.; Chhowalla, M.; Tretiak, S.; Alam, M. A.; Wang, H.-L.; Mohite, A. D. Solar Cells. High-Efficiency Solution-Processed Perovskite Solar Cells with Millimeter-Scale Grains. *Science* **2015**, *347*, 522−525.
(22) Chen, J.; Zhao, X.; Kim, S.-G.; Park, N.-G. Multifunctional Chemical Linker Imidazoleacetic Acid Hydrochloride for 21% Efficient and Stable Planar Perovskite Solar Cells. *Adv. Mater.* **2019**, *31*, No. 1902902.
(23) Son, D. Y.; Lee, J. W.; Choi, Y. J.; Jang, I. H.; Lee, S.; Yoo, P. J.; Shin, H.; Ahn, N.; Choi, M.; Kim, D.; Park, N. G. Self-Formed Grain Boundary Healing Layer for Highly Efficient CH3 NH3 PbI3 Perovskite Solar Cells. *Nat. Energy* **2016**, *1*, No. 16081.
(24) Braly, I. L.; deQuilettes, D. W.; Pazos-Outón, L. M.; Burke, S.; Ziffer, M. E.; Ginger, D. S.; Hillhouse, H. W. Hybrid Perovskite Films Approaching the Radiative Limit with over 90% Photoluminescence Quantum Efficiency. *Nature Photon* **2018**, *12*, 355−361.
(25) Grévin, B. *Kelvin Probe Force Microscopy Characterization of Organic and Hybrid Perovskite Solar Cells*; Springer, 2018.
(26) Bergmann, V. W.; Guo, Y.; Tanaka, H.; Hermes, I. M.; Li, D.; Klasen, A.; Bretschneider, S. A.; Nakamura, E.; Berger, R.; Weber, S. A. L. Local Time-Dependent Charging in a Perovskite Solar Cell. *ACS Appl. Mater. Interfaces* **2016**, *8*, 19402−19409.
(27) Bergmann, V. W.; Weber, S. A. L.; Javier Ramos, F.; Nazeeruddin, M. K.; Grätzel, M.; Li, D.; Domanski, A. L.; Lieberwirth, I.; Ahmad, S.; Berger, R. Real-Space Observation of Unbalanced Charge Distribution inside a Perovskite-Sensitized Solar Cell. *Nat. Commun.* **2014**, *5*, No. 5001.
(28) Garrett, J. L.; Tennyson, E. M.; Hu, M.; Huang, J.; Munday, J. N.; Leite, M. S. Real-Time Nanoscale Open-Circuit Voltage Dynamics of Perovskite Solar Cells. *Nano Lett.* **2017**, *17*, 2554−2560.
(29) Moerman, D.; Eperon, G. E.; Precht, J. T.; Ginger, D. S. Correlating Photoluminescence Heterogeneity with Local Electronic Properties in Methylammonium Lead Tribromide Perovskite Thin Films. *Chem. Mater.* **2017**, *29*, 5484−5492.
(30) Yun, J. S.; Ho-Baillie, A.; Huang, S.; Woo, S. H.; Heo, Y.; Seidel, J.; Huang, F.; Cheng, Y.-B.; Green, M. A. Benefit of Grain Boundaries in Organic-Inorganic Halide Planar Perovskite Solar Cells. *J. Phys. Chem. Lett.* **2015**, *6*, 875−880.
(31) She, L.; Liu, M.; Zhong, D. Atomic Structures of CH3NH3PbI3 (001) Surfaces. *ACS Nano* **2016**, *10*, 1126−1131.
(32) Kim, D.; Yun, J.-H.; Lyu, M.; Kim, J.; Lim, S.; Yun, J. S.; Wang, L.; Seidel, J. Probing Facet-Dependent Surface Defects in MAPbI3 Perovskite Single Crystals. *J. Phys. Chem. C* **2019**, *123*, 14144−14151.
(33) Harwell, J. R.; Baikie, T. K.; Baikie, I. D.; Payne, J. L.; Ni, C.; Irvine, J. T. S.; Turnbull, G. A.; Samuel, I. D. W. Probing the Energy Levels of Perovskite Solar Cells via Kelvin Probe and UV Ambient Pressure Photoemission Spectroscopy. *Phys. Chem. Chem. Phys.* **2016**, *18*, 19738−19745.
(34) Stecker, C.; Liu, K.; Hieulle, J.; Ohmann, R.; Liu, Z.; Ono, L. K.; Wang, G.; Qi, Y. Surface Defect Dynamics in Organic-Inorganic Hybrid Perovskites: From Mechanism to Interfacial Properties. *ACS Nano* **2019**, *13*, 12127−12136.
(35) Gallet, T.; Grabowski, D.; Kirchartz, T.; Redinger, A. Fermi-Level Pinning in Methylammonium Lead Iodide Perovskites. *Nanoscale* **2019**, *11*, 16828−16836.
(36) Yin, W.-J.; Shi, T.; Yan, Y. Unusual Defect Physics in CH3NH3PbI3 Perovskite Solar Cell Absorber. *Appl. Phys. Lett.* **2014**, *104*, No. 063903.
(37) Du, M. H. Efficient Carrier Transport in Halide Perovskites: Theoretical Perspectives. *J. Mater. Chem. A* **2014**, *2*, 9091−9098.
(38) Colchero, J.; Gil, A.; Baró, A. M. Resolution Enhancement and Improved Data Interpretation in Electrostatic Force Microscopy. *Phys. Rev. B* **2001**, *64*, No. 245403.
(39) Si, H.; Zhang, S.; Ma, S.; Xiong, Z.; Kausar, A.; Liao, Q.; Zhang, Z.; Sattar, A.; Kang, Z.; Zhang, Y. Emerging Conductive Atomic Force Microscopy for Metal Halide Perovskite Materials and Solar Cells. *Adv. Energy Mater.* **2020**, *10*, No. 1903922.
(40) Lee, J.-W.; Bae, S.-H.; Hsieh, Y.-T.; De Marco, N.; Wang, M.; Sun, P.; Yang, Y. A Bifunctional Lewis Base Additive for Microscopic Homogeneity in Perovskite Solar Cells. *Chem* **2017**, *3*, 290−302.
(41) Zhang, W.; Pathak, S.; Sakai, N.; Stergiopoulos, T.; Nayak, P. K.; Noel, N. K.; Haghighirad, A. A.; Burlakov, V. M.; deQuilettes, D. W.; Sadhanala, A.; Li, W.; Wang, L.; Ginger, D. S.; Friend, R. H.; Snaith, H. J. Enhanced Optoelectronic Quality of Perovskite Thin Films with Hypophosphorous Acid for Planar Heterojunction Solar Cells. *Nat. Commun.* **2015**, *6*, No. 10030.
(42) Zhang, W.; Saliba, M.; Moore, D. T.; Pathak, S. K.; Hörantner, M. T.; Stergiopoulos, T.; Stranks, S. D.; Eperon, G. E.; Alexander-Webber, J. A.; Abate, A.; Sadhanala, A.; Yao, S.; Chen, Y.; Friend, R. H.; Estroff, L. A.; Wiesner, U.; Snaith, H. J. Ultrasmooth Organic-Inorganic Perovskite Thin-Film Formation and Crystallization for Efficient Planar Heterojunction Solar Cells. *Nat. Commun.* **2015**, *6*, No. 6142.
(43) Ahmad, Z.; Najeeb, M. A.; Shakoor, R. A.; Alashraf, A.; Al-Muhtaseb, S. A.; Soliman, A.; Nazeeruddin, M. K. Instability in CH 3

https://dx.doi.org/10.1021/acsanm.0c01687
ACS Appl. Nano Mater. 2020, 3, 8268−8277

NH 3 PbI 3 Perovskite Solar Cells Due to Elemental Migration and Chemical Composition Changes. *Sci. Rep.* **2017**, *7*, No. 15406.
(44) Stoumpos, C. C.; Malliakas, C. D.; Kanatzidis, M. G. Semiconducting Tin and Lead Iodide Perovskites with Organic Cations: Phase Transitions, High Mobilities, and Near-Infrared Photoluminescent Properties. *Inorg. Chem.* **2013**, *52*, 9019−9038.
(45) Docampo, P.; Hanusch, F. C.; Giesbrecht, N.; Angloher, P.; Ivanova, A.; Bein, T. Influence of the Orientation of Methylammonium Lead Iodide Perovskite Crystals on Solar Cell Performance. *APL Mater.* **2014**, *2*, No. 081508.
(46) Kim, H.-S.; Lee, C.-R.; Im, J.-H.; Lee, K.-B.; Moehl, T.; Marchioro, A.; Moon, S.-J.; Humphry-Baker, R.; Yum, J.-H.; Moser, J. E.; Grätzel, M.; Park, N.-G. Lead Iodide Perovskite Sensitized All-Solid-State Submicron Thin Film Mesoscopic Solar Cell with Efficiency Exceeding 9%. *Sci. Rep.* **2012**, *2*, No. 591.
(47) Caputo, M.; Cefarin, N.; Radivo, A.; Demitri, N.; Gigli, L.; Plaisier, J. R.; Panighel, M.; Di Santo, G.; Moretti, S.; Giglia, A.; Polentarutti, M.; De Angelis, F.; Mosconi, E.; Umari, P.; Tormen, M.; Goldoni, A. Electronic Structure of MAPbI 3 and MAPbCl 3: Importance of Band Alignment. *Sci. Rep.* **2019**, *9*, No. 15159.
(48) Endres, J.; Egger, D. A.; Kulbak, M.; Kerner, R. A.; Zhao, L.; Silver, S. H.; Hodes, G.; Rand, B. P.; Cahen, D.; Kronik, L.; Kahn, A. Valence and Conduction Band Densities of States of Metal Halide Perovskites: A Combined Experimental−Theoretical Study. *J. Phys. Chem. Lett.* **2016**, *7*, 2722−2729.
(49) Tao, S.; Schmidt, I.; Brocks, G.; Jiang, J.; Tranca, I.; Meerholz, K.; Olthof, S. Absolute Energy Level Positions in Tin- and Lead-Based Halide Perovskites. *Nat. Commun.* **2019**, *10*, No. 2560.
(50) Rhoderick, E. H.; Williams, R. H. *Metal-Semiconductor Contacts*; Clarendon Press; Oxford University Press: Oxford [England]; New York, 1988.
(51) de Quilettes, D. W.; Vorpahl, S. M.; Stranks, S. D.; Nagaoka, H.; Eperon, G. E.; Ziffer, M. E.; Snaith, H. J.; Ginger, D. S. Impact of Microstructure on Local Carrier Lifetime in Perovskite Solar Cells. *Science* **2015**, *348*, 683−686.
(52) Shi, L. X.; Wang, Z. S.; Huang, Z.; Sha, W. E. I.; Wang, H.; Zhou, Z. The Effects of Interfacial Recombination and Injection Barrier on the Electrical Characteristics of Perovskite Solar Cells. *AIP Adv.* **2018**, *8*, No. 025312.
(53) Jiménez-López, J.; Cambarau, W.; Cabau, L.; Palomares, E. Charge Injection, Carriers Recombination and HOMO Energy Level Relationship in Perovskite Solar Cells. *Sci. Rep.* **2017**, *7*, No. 61016101.
(54) Dharmadasa, I. M. Fermi Level Pinning and Effects on CuInGaSe2-Based Thin-Film Solar Cells. *Semicond. Sci. Technol.* **2009**, *24*, No. 055016.
(55) Colleoni, D.; Miceli, G.; Pasquarello, A. Fermi-Level Pinning through Defects at GaAs/Oxide Interfaces: A Density Functional Study. *Phys. Rev. B* **2015**, *92*, No. 125304.
(56) Mosconi, E.; Azpiroz, J. M.; De Angelis, F. Ab Initio Molecular Dynamics Simulations of Methylammonium Lead Iodide Perovskite Degradation by Water. *Chem. Mater.* **2015**, *27*, 4885−4892.
(57) Haruyama, J.; Sodeyama, K.; Han, L.; Tateyama, Y. Termination Dependence of Tetragonal CH3NH3PbI3 Surfaces for Perovskite Solar Cells. *J. Phys. Chem. Lett.* **2014**, *5*, 2903−2909.
(58) Quarti, C.; De Angelis, F.; Beljonne, D. Influence of Surface Termination on the Energy Level Alignment at the CH3NH3PbI3 Perovskite/C60 Interface. *Chem. Mater.* **2017**, *29*, 958−968.
(59) Li, Y.; Xu, X.; Wang, C.; Wang, C.; Xie, F.; Yang, J.; Gao, Y. Degradation by Exposure of Coevaporated CH3NH3PbI3 Thin Films. *J. Phys. Chem. C* **2015**, *119*, 23996−24002.
(60) Koocher, N. Z.; Saldana-Greco, D.; Wang, F.; Liu, S.; Rappe, A. M. Polarization Dependence of Water Adsorption to CH3NH3PbI3 (001) Surfaces. *J. Phys. Chem. Lett.* **2015**, *6*, 4371−4378.
(61) Ralaiarisoa, M.; Salzmann, I.; Zu, F.-S.; Koch, N. Effect of Water, Oxygen, and Air Exposure on CH3NH3PbI3−XClx Perovskite Surface Electronic Properties. *Adv. Electron. Mater.* **2018**, *4*, No. 1800307.
(62) Yin, W.-J.; Shi, T.; Yan, Y. Unique Properties of Halide Perovskites as Possible Origins of the Superior Solar Cell Performance. *Adv. Mater.* **2014**, *26*, 4653−4658.
(63) Wei, S.-H. Overcoming the Doping Bottleneck in Semiconductors. *Comput. Mater. Sci.* **2004**, *30*, 337−348.
(64) Wang, Q.; Shao, Y.; Xie, H.; Lyu, L.; Liu, X.; Gao, Y.; Huang, J. Qualifying Composition Dependent p and n Self-Doping in CH3NH3PbI3. *Appl. Phys. Lett.* **2014**, *105*, No. 163508.
(65) Wang, Q.; Shao, Y.; Dong, Q.; Xiao, Z.; Yuan, Y.; Huang, J. Large Fill-Factor Bilayer Iodine Perovskite Solar Cells Fabricated by a Low-Temperature Solution-Process. *Energy Environ. Sci.* **2014**, *7*, 2359−2365.
(66) Heo, J. H.; Im, S. H.; Noh, J. H.; Mandal, T. N.; Lim, C.-S.; Chang, J. A.; Lee, Y. H.; Kim, H.; Sarkar, A.; Nazeeruddin, M. K.; Grätzel, M.; Seok, S. I. Efficient Inorganic−Organic Hybrid Heterojunction Solar Cells Containing Perovskite Compound and Polymeric Hole Conductors. *Nat. Photonics* **2013**, *7*, 486−491.
(67) Kim, H.-S.; Mora-Sero, I.; Gonzalez-Pedro, V.; Fabregat-Santiago, F.; Juarez-Perez, E. J.; Park, N.-G.; Bisquert, J. Mechanism of Carrier Accumulation in Perovskite Thin-Absorber Solar Cells. *Nat. Commun.* **2013**, *4*, No. 2242.
(68) Huang, Z.; Wang, D.; Wang, S.; Zhang, T. Highly Efficient and Stable MAPbI3 Perovskite Solar Cell Induced by Regulated Nucleation and Ostwald Recrystallization. *Materials* **2018**, *11*, No. 778.
(69) Troughton, J.; Hooper, K.; Watson, T. M. Humidity Resistant Fabrication of CH3NH3PbI3 Perovskite Solar Cells and Modules. *Nano Energy* **2017**, *39*, 60−68.
(70) Beamson, G. High Resolution XPS of Organic Polymers. The Scienta ESCA 300 Database 1992.
(71) Hoehn, R. D.; Francisco, J. S.; Kais, S.; Kachmar, A. Role of Water on the Rotational Dynamics of the Organic Methylammonium Cation: A First Principles Analysis. *Sci. Rep.* **2019**, *9*, No. 668.
(72) Turton, R. J. *The Physics of Solids*; Oxford University Press: Oxford, New York, 2000.
(73) Desbief, S.; Hergué, N.; Douhéret, O.; Surin, M.; Dubois, P.; Geerts, Y.; Lazzaroni, R.; Leclère, P. Nanoscale Investigation of the Electrical Properties in Semiconductor Polymer−Carbon Nanotube Hybrid Materials. *Nanoscale* **2012**, *4*, 2705−2712.

https://dx.doi.org/10.1021/acsanm.0c01687
ACS Appl. Nano Mater. 2020, 3, 8268−8277